NeuroImage **14,** 1058–1069 (2001)
doi:10.1006/nimg.2001.0906, available online at http://www.idealibrary.com on IDEAL®

Validating Cortical Surface Analysis of Medial Prefrontal Cortex

J. T. Ratnanather,*,[1] K. N. Botteron,† T. Nishino,† A. B. Massie,* R. M. Lal,* S. G. Patel,*
S. Peddi,* R. D. Todd,† and M. I. Miller*

**Center for Imaging Science, The Johns Hopkins University, Baltimore, Maryland 21218-2686; and †Department of Psychiatry, Washington University School of Medicine, St. Louis, Missouri 63110*

Received January 30, 2001

This paper describes cortical analysis of 19 high resolution MRI subvolumes of medial prefrontal cortex (MPFC), a region that has been implicated in major depressive disorder. An automated Bayesian segmentation is used to delineate the MRI subvolumes into cerebrospinal fluid (CSF), gray matter (GM), white matter (WM), and partial volumes of either CSF/GM or GM/WM. The intensity value at which there is equal probability of GM and GM/WM partial volume is used to reconstruct MPFC cortical surfaces based on a 3-D isocontouring algorithm. The segmented data and the generated surfaces are validated by comparison with hand segmented data and semiautomated contours, respectively. The L_1 distances between Bayesian and hand segmented data are 0.05–0.10 ($n = 5$). Fifty percent of the voxels of the reconstructed surface lie within 0.12–0.28 mm ($n = 14$) from the semiautomated contours. Cortical thickness metrics are generated in the form of frequency of occurrence histograms for GM and WM labelled voxels as a function of their position from the cortical surface. An algorithm to compute the surface area of the GM/WM interface of the MPFC subvolume is described. These methods represent a novel approach to morphometric chacterization of regional cortex features which may be important in the study of psychiatric disorders such as major depression.

INTRODUCTION

Major depressive disorder is recognized to be a common, impairing, and frequently recurrent illness with significant public health impact. As detailed in the Global Burden of Disease study, major depressive disorder ranked second in disease incidence and third in disability adjusted life years, where one disability adjusted life year is defined as the loss of 1 year of healthy life to disease (Murray and Lopez, 1996). A variety of recent functional and structural neuroimaging studies of both normal affect regulation and differences associated with affective disorders such as major depressive disorder or bipolar affective disorder, implicate specific limbic circuits involving the ventral and medial prefrontal cortex, along with subcortical limbic structures such as the amygdala and related parts of the striatum and thalamus in the pathophysiology of depression (reviewed in Swerdlow and Koob, 1987; Drevets *et al.*, 1992; Drevets and Todd, 1997; Botteron and Figiel, 1997; Drevets, 1999). For example, in clinically ascertained depressed adults cerebral blood flow and metabolism are increased in the ventral prefrontal cortex, the amygdala and the medial thalamus while flow is reduced in the medial caudate and subgenual prefrontal cortex (Drevets, 1999). Several studies have reported that structures in these specific limbic circuits may be reduced or increased in volume in adults with a history of major depressive disorder or bipolar affective disorder. Although there are some conflicting results reported for structural brain changes in affective disorders, recent critical reviews (Botteron and Figiel, 1997; Drevets and Botteron, 1996; Drevets and Todd, 1997; Soares and Mann, 1997) support that major depression is associated with specific neuromorphometric differences and suggest that some conflict in reported studies is probably related to limitations in image acquisition or image analysis in earlier studies. Although recent advances in MRI technology and image analysis have allowed for the more precise volumetric definition of smaller and more anatomically relevant regions than was possible even 5 years ago, the majority of the studies involving the structure of specific prefrontal or limbic regions in major depression have been reported for small subject numbers over limited anatomical regions. These limitations are largely related to the difficulty and labor intensity required by skilled raters for regionally specific or anatomically relevant measures. Medial and ventral or orbital prefrontal regions have not been rigorously studied with robust automated methods which are sensitive to detailed regional neuroanatomy. Given the public health burden of depression and the increased resolution in neuroimaging,

---

[1] To whom correspondence and reprint requests should be addressed. Fax: (410) 516-4594. E-mail: tilak@cis.jhu.edu.

1053-8119/01 $35.00

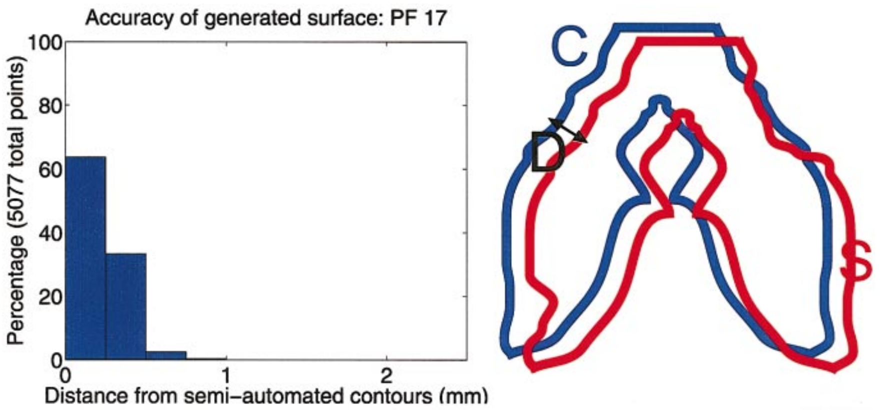

FIG. 1. Left panel shows the histogram generated when the semi-automated contours are compared with the corresponding sections across the automated surface for brain PF17. Right panel shows the schematic of the algorithm. C is the semiautomated contour; S is the boundary of the surface; and D is the distance between C and S.

detailed cortical analysis of structural brain changes in depression appears opportune.

We have chosen to focus our methods for cortex extraction and automated surface construction in ventral medial prefrontal and orbital frontal regions given the accumulating evidence of their importance in major depression including differences in regional blood flow and glucose metabolism (Drevets *et al.*, 1997; Drevets, 1999; Mayberg *et al.*, 1999) and strikingly significant gray matter volume reduction in a specific small region of the medial ventral prefrontal cortex known as the subgenual prefrontal cortex (Drevets *et al.*, 1997; Hirayasu *et al.*, 1999; Botteron *et al.*, 2001). Postmortem neuropathology studies have also supported that there are structural changes in these regions potentially related to underlying changes in neuronal size and glial number (Ongur *et al.*, 1998; Rajkowska *et al.*, 1999).

Increased resolution in neuroimaging now makes it possible to perform precise neuromorphometric analysis of smaller brain regions such as the medial prefrontal cortex (MPFC) using tools developed in the emerging field of Computational Anatomy (Grenander and Miller, 1998). In particular, tools which analyze the exquisite macroscopic features of the neocortical surface along with the cortical mantle composing of gray matter are now available (Dale and Sereno, 1993; Kapur *et al.*, 1996; Thompson *et al.*, 1996; Drury *et al.*, 1996; van Essen *et al.*, 1998; Teo *et al.*, 1997; Bakircioglu *et al.*, 1998; Khaneja *et al.*, 1998; Bakircioglu *et al.*, 1999; Joshi *et al.*, 1999; Prince *et al.*, 1999; Miller *et al.*, 2000).

In general, there are two central components to the analysis of the neocortex: (i) the construction of the 3-D neocortical mantle representing the positions of the gray matter connected voxels forming the highly curved structure, and (ii) the construction of a triangulated graph representing the 2-D manifold of the midlayer 4 boundary, the gray/white matter boundary, or the gray/cerebrospinal fluid boundary. These two components (i) and (ii) are linked in that the 2-D manifold of the surface, and therefore its curved geometry, are determined by the variation, position, and density of the cortical mantle cells, manifested as gray matter at the macroscopic scale of current MRI imaging methods.

We focus our attention on the properties of the 3-D neocortical mantle of the MPFC, namely the relative frequency occurrences of the gray matter (GM), white matter (WM), and cerebrospinal fluid (CSF) compartments as a function of the location in an image with respect to the cortical surface. Building on the methods described previously (Joshi *et al.*, 1999; Miller *et al.*, 2000), we characterize statistical variations in the 3-D cortical mantle as manifested by volume and thickness changes. We also describe an improved algorithm that computes the distance between a given voxel and the generated cortical surface for calculating the covariation statistics.

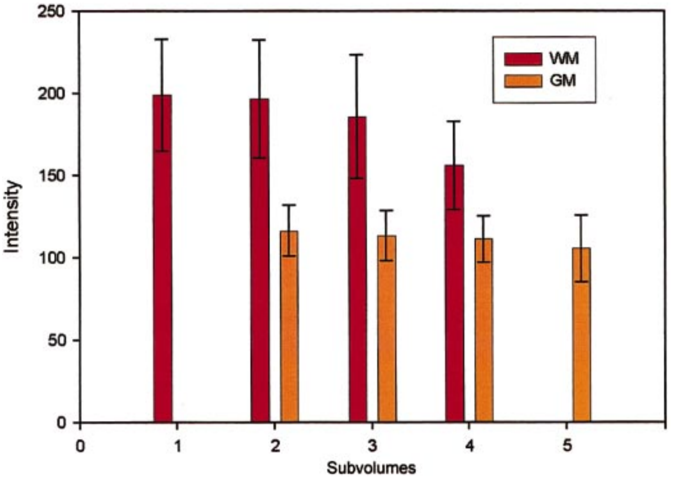

FIG. 2. Axial variation of GM and WM mean intensities across five subvolumes of PF15–PF19 brains from superior end (1) toward inferior end (5). At each section, left bar denotes mean WM intensity with the standard deviation shown in error bar and right bar denotes the corresponding case for GM.

The highly curved geometry of the MPFC makes manual morphometric analysis difficult and labor intensive. Hence the need to demonstrate the validity and effectiveness of the semiautomated tools developed previously and now adapted for a significantly large set of MPFC subvolumes. Additionally, the traditional description of volume alone does not adequately characterize the neuromorphometry of cortical regions of interest. The automated methods described here address the issue of feasibility and begin to further quantitatively describe regional neuromorphometry. Ultimately, results accrued from such an extensive morphometric analysis will be useful in analyzing changes in the MPFC associated with major depressive disorders and other psychiatric disorders.

METHODS

Subjects/Data Sets

For the refinement and testing of the algorithms described in this work, analyses were completed on MR images from a total of 19 subjects. Subjects were young adult female twins who are participants in a larger epidemiologic twin imaging study investigating neuromorphometry associated with major depression. Brain images from the 19 subjects were divided into two groups for this paper. The first set of brains analyzed were the five subjects labeled PF15 to PF19. This group of five scans were analyzed to examine the validity of the automated tissue classification and surface reconstruction in comparison to manual segmentations completed by an expert rater. The second set of 14 brains labeled PF1–PF14 were used to examine the robustness and characteristics of the automated methods described in this paper and to examine the validity of the methods in comparison to semiautomated image analysis methods.

Data Acquisition and Image Preprocessing

MR images were obtained with a Siemens Vision 1.5T scanner. For each subject, a series of three T1-weighted MPRage sequences was acquired with excitation times of 10–11 ms and relaxation times of 3–4 ms. Whole brain acquisitions were obtained sagittally with a Field of View (FOV) of 256 × 256 using 160 sections with isotropic 1 × 1 × 1 mm voxels. The three image acquisitions were registered using subroutines in Analyze (Robb, 1999), summed, and then interpolated giving a final resolution of 0.5 mm isotropic voxels. Summing the 3 MPRage acquisitions results in improved signal to noise characteristics in the image (Holmes *et al.*, 1998) and improved GM/WM boundary discrimination. Resampling allows for more precise definition of segmentation and surface boundaries (Haller *et al.*, 1997).

The dynamic range of the images was defined by fitting the image intensity histogram with Gaussian curves representing the WM peak and CSF peak. Let $h \in \{\text{GM}, \text{WM}, \text{CSF}, \text{CSF/GM-PV}, \text{GM/WM-PV}\}$ be the hypothesis labels, and μ_h and σ_h be, respectively, the mean and standard deviation corresponding to the Gaussian curves. The images were then rescaled to an 8-bit scale (0–255) range using intensity ranges $[0, \mu_{\text{WM}} + 4\sigma_{\text{WM}}]$ for brains PF1–PF14 and $[\mu_{\text{CSF}} - 2\sigma_{\text{CSF}}, \mu_{\text{WM}} + 2\sigma_{\text{WM}}]$ for brains PF15–PF19.

Since the focus of our efforts were to develop and test methods which could be potentially applied to smaller specific cerebral regions, subregions were defined for subsequent analysis. We initially defined a small region of the ventral medial prefrontal cortex for brains PF15–PF19. For the purpose of methods development and validation analysis of the automated cortical analysis methods, these subregions were loosely specified to be overinclusive of potentially interesting anatomically relevant regions. The primary ROI, the MPFC, is included as a portion of these regional definitions.

For the manual expert rater validation set (PF15–PF19), the region was defined, in the anterior–posterior direction, as starting five sections posterior to the rostral end of the subgenual portion of the cingulate gyrus and ending five sections anterior to the corpus callosum. Laterally PF15–PF19 were delimited by the olfactory sulcus. The PF15–PF19 brains represented the initial application of the auto-segmentation which revealed high sensitivity to the number of voxels. The region was too narrowly defined resulting in marginally adequate voxel numbers to calculate valid statistics for the Bayesian segmentation. Therefore, in PF1–PF14 a more generous region was defined which was still localized enough to maintain uniform statistics.

In this analysis the images were not reoriented to a standard position prior to application of the automated cortical analysis methods. Reorientation results in a loss of high frequency signal information related to interpolation. In our approach, in order to maximize the ability to discriminate tissue classification and boundary definition, reorientation to a standard position occurs after the cortical image processing.

Manual Segmentation

The initial set of PF15–PF19 subvolumes were hand segmented into CSF, CSF/GM-PV, GM, and WM compartments (where PV denotes partial volume). This was completed by an expert (KNB) who was aware of the methods being validated, but did not view the automated methods that were done in a remote location. Hand segmentation was based on a study of the neuroanatomy through cryosection samples and atlases and extensive experience with manual measures from this region. Voxel classification by the expert was

TABLE 1

L_1 Distance for GM- and WM-labeled Voxels Obtained from Multisubvolume EM Calibration

	GM			WM			GM & WM
Brain	Hand	Bayes	L_1	Hand	Bayes	L_1	L_1
PF15	25839	24156	0.07	26767	25280	0.06	0.06
PF16	36358	34413	0.05	28877	27470	0.05	0.05
PF17	17445	17164	0.02	21612	18428	0.15	0.09
PF18	24417	21231	0.13	21859	20539	0.06	0.10
PF19	24435	23084	0.06	23945	21915	0.08	0.07

Note. Columns 2–4, respectively, show the number of hand segmented voxels, Bayesian segmented voxels, and the L_1 distance for GM voxels. Columns 5–7, respectively, show the number of hand segmented voxels, Bayesian segmented voxels, and the L_1 distance for WM voxels. Column 8 shows the corresponding L_1 distance for the combined GM- and WM-labeled voxels.

based on visual inspection of morphological cues such as gyri curvature and connectivity, as well as visual intensity cues between GM, WM, and CSF.

Semiautomated Contour Generation

Using the Analyze software (Robb, 1999), contours were generated at the interface of GM–WM boundary in each of the coronal sections of the MRI data. Specifically, the WM was segmented by seeding and thresholding. Each section was examined and edited from which the contour was generated. Then each contour was adjusted by a single rater to overlay the GM/WM boundary based on visual examination.

Bayesian Segmentation

The MRI data is segmented into M compartments using the Bayesian segmentation algorithm developed by Joshi *et al.* (1999) and Miller *et al.* (2000), extending the work of Teo *et al.* (1997). The expectation–maximization (EM) algorithm is used to locally fit the parameters of the mixture densities throughout the MRI data analogous to Kapur *et al.* (1996).

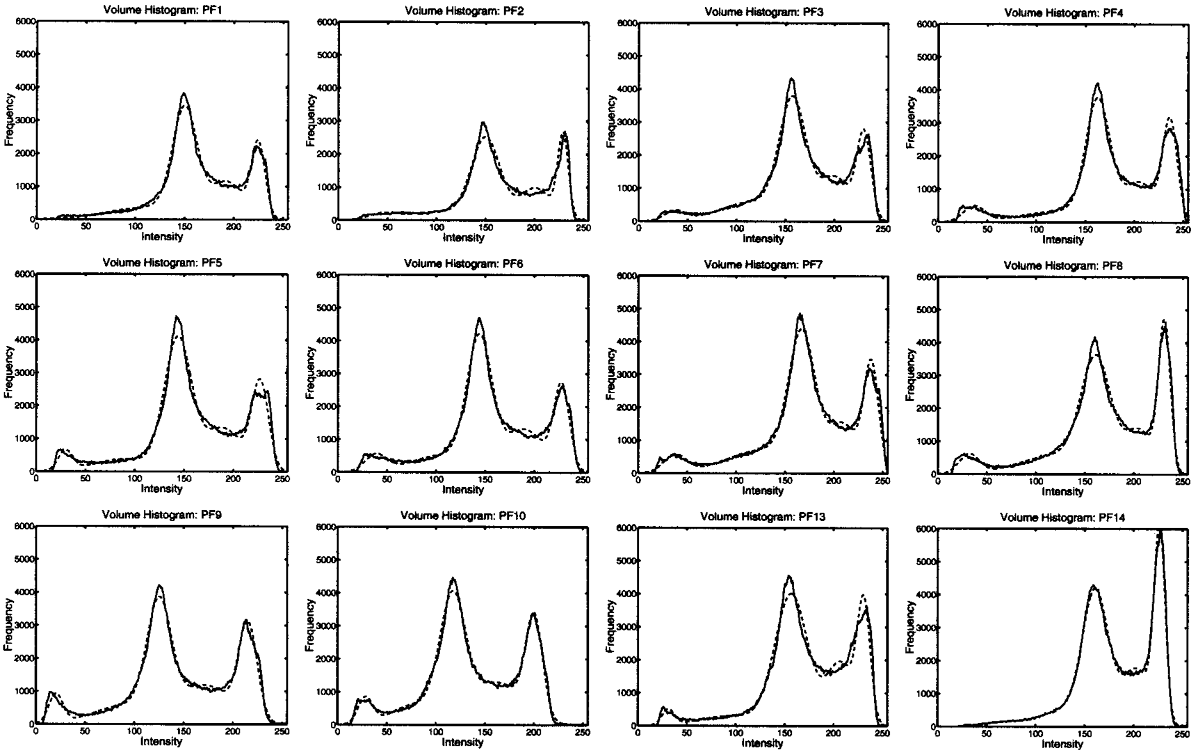

FIG. 3. Bayesian histogram fitting of PF1–PF10, PF13–PF14. Continuous line represents raw data while dashed line represents fitted data.

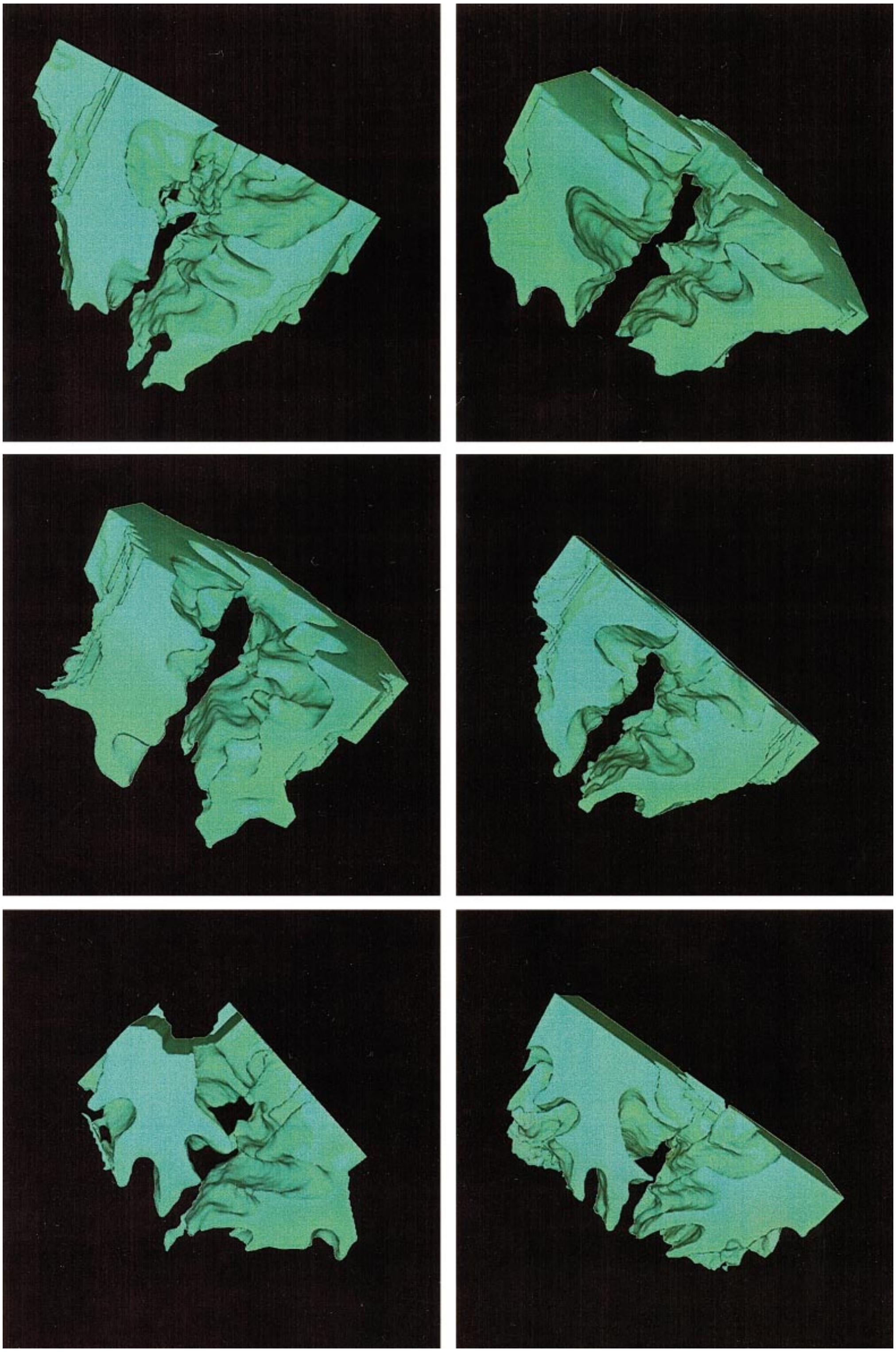

FIG. 4. Reconstructed surfaces. Row 1, PF5–PF6; Row 2, PF7–PF8; Row 3, PF13–PF14. Surfaces were generated by the isocontoring algorithm using the threshold between the GM and GM/WM PV compartments. The view shown here is in the Anterior–Posterior direction.

Let Ω be a discrete lattice, with coordinates x_n, $n = 1, \ldots, N$ constituting the image volume. The MRI data is a function $I : \Omega \rightarrow \mathbb{R}^m$ is defined for multiple modalities. Let $h \in \mathcal{H}$, which is the space of anatomical labels so that $h \triangleq \{h_n, n = 1, \ldots, N\}$, $h_n \in \{H_1, H_2, \ldots\}$. Assume the simple statistical mixture model of conditional Gaussian data for I with compartment types $\{H_1, H_2, \ldots\}$ with means and variances μ_n, σ_n^2 a function of position $n = 1, \ldots, N$ with $\pi(h)$ the prior distribution representing the relative amount of the five compartments. The optimal Bayes maximum a-posteriori segmentation generates the labels according to Algorithm 1 described below.

Algorithm 1: Bayesian Segmentation Algorithm

```
for all label $n$ do
    $\hat{h}_n = \arg\max_{h_n \in \mathcal{H}} \sum_{n=1}^{N} \left( -\frac{1}{2} \log 2\pi\sigma_n^2(h_n) - \frac{1}{2} \frac{(I_n - \mu_n(h_n))^2}{\sigma_n^2(h_n)} + \log \pi(h_n) \right)$
end for
```

Segmentation Accuracy

The accuracy of the automated Bayesian segmentation is assessed by comparison with the manual segmentation. Let $\mathcal{M}$ be a manual segmentation of the image such that each of the M compartments is labeled with a tag from 1 to M (zero represents areas of the volume which are not segmented, for instance the background). Further, $\mathcal{A}$ is an M compartment automated segmentation with the same labeling scheme as the reference manual segmentation. Let $p^{\mathcal{A}}(h_n|I)$ be the a posteriori probability of hypothesis h_n at voxel n, and $p^{\mathcal{M}}(h_n|I)$ be the *a posteriori* probability of hypothesis h_n at the same voxel for the manual segmentation. Generally, this will have a value of either 1 or 0, unless the manual rater assigns partial volume numbers to the compartment. The L_1 distance between the two segmentations is:

$$\frac{1}{2N} \sum_{n=1}^{N} \sum_{m=1}^{M} |p^{\mathcal{A}}(h_n = H_m|I) - p^{\mathcal{M}}(h_n = H_m|I)|. \quad (1)$$

Surface Reconstruction

The Bayesian segmentation is used to reconstruct the corresponding cortical surface. We use isosurface generation to generate the triangulated graphs representing the cortical surface. The Gueziec and Hummel (1995) algorithm is used to generate a tessellation of triangles for an isosurface of a given intensity. Each voxel (eight points) is decomposed into five tetrahedra. The resulting surface is a triangulation made up of the triangles that bound these tetrahedra.

Cortical Thickness Metrics

As described in Miller *et al.* (2000), we examine the variation of GM, WM, and CSF voxels as a function of their position from the generated cortical surface. This requires computing the distance between the voxels in the segmented image and the cortical surface. For each voxel in the segmented image with a nonzero intensity, the vertex in the triangulated surface closest to that voxel is calculated, and the distance between the vertex and the voxel is measured. This distance increments a histogram associated with its GM, WM, or CSF label. For every voxel examined, we first determine the point in the middle of the cube the voxel represents. The cortical thickness metric is computed

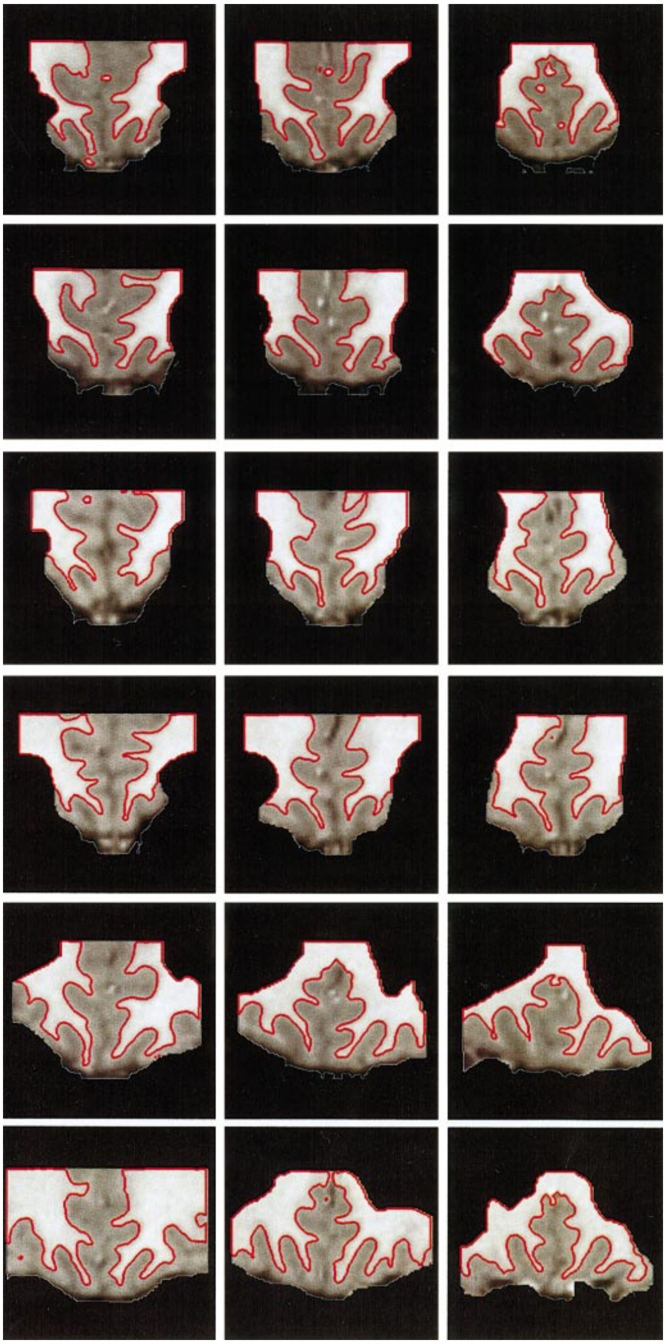

FIG. 5. For brains PF5–PF6, PF7–PF8, and PF13–PF14, the respective row corresponds to three coronal sections of embedded surface.

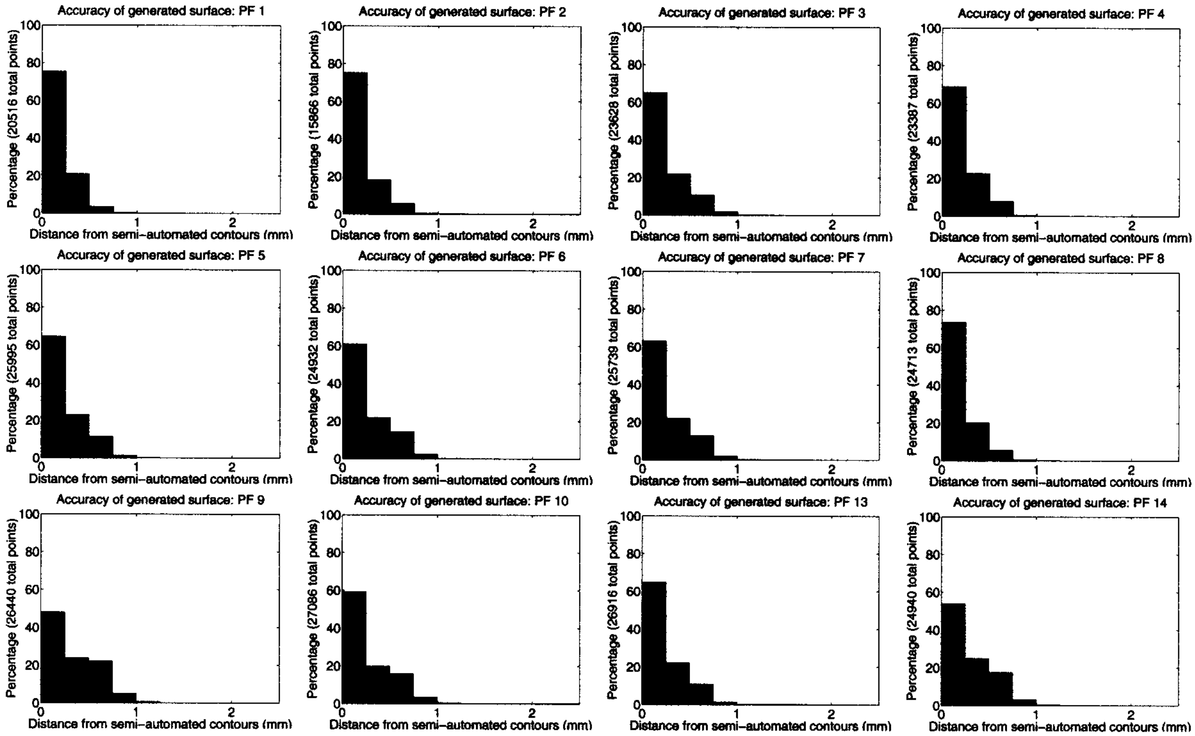

Accuracy of generated surface: PF 1

Accuracy of generated surface: PF 2

Accuracy of generated surface: PF 3

Accuracy of generated surface: PF 4

Accuracy of generated surface: PF 5

Accuracy of generated surface: PF 6

Accuracy of generated surface: PF 7

Accuracy of generated surface: PF 8

Accuracy of generated surface: PF 9

Accuracy of generated surface: PF 10

Accuracy of generated surface: PF 13

Accuracy of generated surface: PF 14

FIG. 6. Each bar graph is a histogram comparing a generated surface with a semiautomated contour. The graphs show the number of points in the contour at a given distance from the surface in 1/4-mm intervals. Data correspond to brains PF1–PF10 and PF13–PF14.

using Algorithm 2 described in Appendix A. Finding the closest point on the surface to the voxel is computationally intensive if we compare the distance between every voxel and every surface point as was the case in Miller *et al.* (2000). Instead we develop a faster and efficient algorithm that uses a OcTree data structure (Sedgwick, 1983) for the surface points so that points are not visited which do not relate to the calculation. This is described in Algorithm 3 in Appendix A.

Surface Reconstruction Validation

To validate the isosurface generation of the MRI data, semiautomated contours are compared to the automatically generated surfaces. For each vertex on every contour, a distance is calculated between it and the generated isosurfaces. If S represents the set of points in the surface and C the set of points in the contour, and D the distances from the points in C to the points in S, we compute D with the following algorithm:

Algorithm 4: Distance Computation

```
for all $C_i \in C$ do
    $S_{\text{closest}} \leftarrow a$ point in $S$ such that
    for all $S_i \in S$ do
        distance $(S_{\text{closest}}, C_i) \leq$ distance $(S_i, C_i)$
    end for
    $D_i \leftarrow$ distant $(S_{\text{closest}}, C_i)$.
end for
```

The median of the distances in D represents the median contour/surface distance, and a histogram of the values of D shows the distribution of the distances. We find S_{closest} by using the tree structure described in Appendix A. We initialize the structure with the points in S and then find the distance to S for each point in C.

In calculating the voxel to surface distance, we are not limited by the resolution of the resampled data. The surface is constructed in the continuum, say the unit cube containing the full brain. Vertices occur at real values in the cube; the set distances represented

TABLE 2

Medians (Expressed in mm) at Which 50% of Voxels of Generated Surface Lie from Semiautomated Contour

Brain	PF1	PF2	PF3	PF4	PF5	PF6	PF7
Median	0.13	0.12	0.13	0.13	0.14	0.15	0.13
Brain	PF8	PF9	PF10	PF11	PF12	PF13	PF14
Median	0.10	0.28	0.17	0.13	0.12	0.14	0.21

by the voxel to surface calculation may be much smaller than the voxel resolution as triangles will generally slice through the voxels. This is represented by the large number of distances well below the voxel resolution. As an illustration, Fig. 1 shows an histogram for PF17 that was reported in Miller *et al.* (2000) together with a schematic of how the semiautomated contour is compared with that from the surface.

Calculating GM/WM Interface Surface Area

To calculate the area of the triangulated graph of the reconstructed surface between GM and WM compartments of the brain, we obtained all triangles whose vertices are in the GM and GM/WM-PV labeled compartments as outlined in Algorithm 5 in Appendix A. To validate the surface area algorithm, we computed the surface area of a prolate semispheroid of gray matter cut out of a cube of white matter and compared it with the known surface area. For a prolate semispheroid of radius $a = 20$ and height $c = 70$, i.e., with a large aspect ratio, we obtained an error of 1% in the surface area calculation.

RESULTS

Segmentation Accuracy

The anatomical location of the MPFC introduces an inhomogeneity in the histogram of GM, WM and CSF voxels in sections in axial direction. Figure 2 shows the mean intensity of the GM and WM segmented voxels as a function of subvolumes of 15 axial sections from the superior end towards the inferior end. Further, the mean WM intensity in the MPFC region was two standard deviation higher than that of the entire brain. This was compensated by increasing the intensity range in normalizing the histogram. The intensity drop-off in the axial direction did not pose a problem in the expert rater manual segmentation because the human rater compensate for the shift. However, for the semiautomated segmentation the intensity change skews the data. Since the intensity histograms in the coronal direction did not show a drift as a function of position, the semi-automated contouring was completed on coronal sections.

For each of the brains PF15–PF19, automated Bayesian segmentation was applied to five axial subvolumes whose histogram excluded voxels that had intensities less than 75. Histograms were fitted with either three compartments pertaining to GM, GM/WM PV, and WM or two corresponding to GM and WM or single corresponding to GM or WM. To assess the accuracy of the Bayesian segmentation, it is necessary to compare with hand segmentation by calculating the L_1 distance between hand and automated GM- and WM-labeled voxels [given by Eq. (1)]. For assigning the partial volume compartment label h^{PV}, if intensity I^{PV} is less than $\mu_{\mathrm{GM/WM-PV}}$, then the label is set to GM, otherwise it is set WM.

Table 1 shows the L_1 distance between the hand and Bayesian segmentation. Columns 2–4, respectively, show the number of hand-labeled voxels, Bayesian-labeled voxels and the L_1 distance for GM. Columns 5–7 show the same data for WM. Column 8 shows the L_1 distance for both GM- and WM-labeled voxels. For comparison, we found that a single segmentation of the whole volume (rather than via five subvolumes) was about 25% less accurate with L_1 distances of 0.08, 0.09, 0.15, 0.09, 0.06, respectively. Incidentally, the histograms of the hand-labeled WM and GM voxels indicate asymmetry with long tails in the PV region. The asymmetry reflects the difficulty in the hand segmentation of voxels in the PV region that represents the highly curved GM/WM interface. Grabowski *et al.* (2000) used information from the partial volumes to perform automated segmentation of MR data; they also observed a bias among six human raters in classifying voxels in the partial volume region. Thus the local parametric fitting obtained from the EM algorithm overcomes the problems caused by different interpretation of a given intensity based on the voxel location in an axial segmentation.

Validating Surface Generation

For the surface analysis, it was found that surfaces and labeled voxels from the single EM calibration of the whole volume histogram were not significantly different from those generated from the subvolumetric EM calibration. Thus, the following surface analysis is based on the results of the single EM calibration. Figure 3 shows the result of Bayesian segmentation of the MR data into CSF, CSF/GM PV, GM, GM/WM PV, and WM compartments for brains PF1–PF10 and PF13–PF14. This figure demonstrates the effectiveness of the local parametric fitting obtained from the EM algorithm.

Figure 4 shows the generated surfaces from three monozygotic twin pairs PF5–PF6, PF7–PF8, and PF13–PF14 where the isocontour was based on the threshold between the GM and GM/WM–PV compartment. Notice the similarities in the shapes of the pair of brains represented in each row. Figure 5 shows coronal sections of the embedded surfaces of the same six brains.

To examine the accuracy of the automated generation of the triangulated graphs representing the GM–WM surface in comparison to semiautomated contours, we calculated the distance between the generated surface and the semiautomated contours. Figure 6 shows that as much as 100% of the voxels on the surface lie within 1 mm from the semiautomated contours. Table 2 compares the surface generated from segmentation with the semiautomated contours by calculating the median distance within which 50% of the

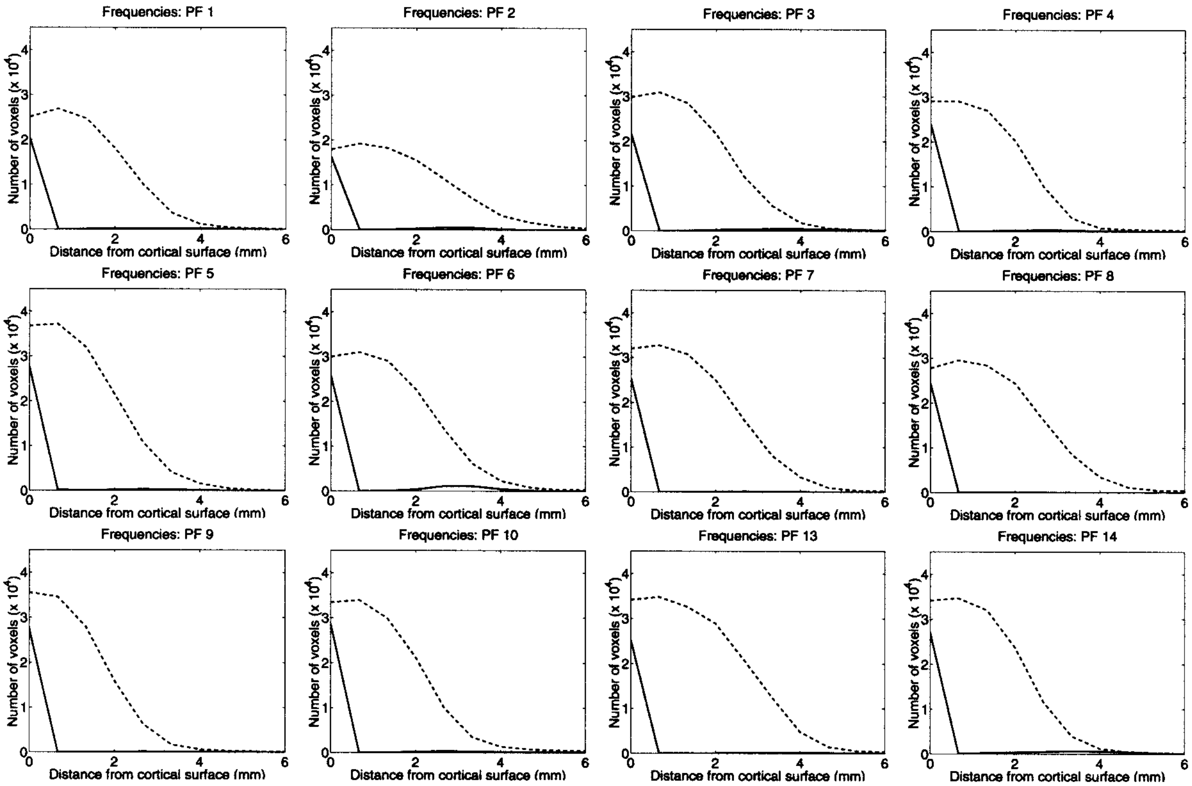

FIG. 7. Cooccurence frequency of voxel assignment as a function of outward distance from the GM/WM boundary for brains PF1–PF10 and PF13–PF14. Straight and dashed lines, respectively, represent white matter and gray matter.

voxels of the generated surface lie. The choice of the threshold between the GM and GM/WM–PV compartments for the isocontour can be construed to enclose all the GM voxels except those adjacent to the highly curved GM/WM interface.

Cortical Thickness Metrics

We now examine the distribution of WM and GM labeled voxels as function of their position along the outward normal of the cortical surface. To compute the empirical covariation of the GM and WM compartments, we calculated the relative frequency of each compartmental hypothesis. This gives a metric of density of each compartment as a function of distance from the surface. Figure 7 shows the frequency profiles of occurrence of WM- and GM-labeled voxels as a function of distance from the GM/WM boundary. Cortical thickness metrics for PF15–PF19 have previously been validated in Miller *et al.* (2000). It is possible to generate localized metrics within user-defined regions of interest. Here we show the metrics for the medial prefrontal cortex.

TABLE 3

Comparison of Surface Area of GM/WM Interface Extracted from Hand and Automated Segmentation

Brain	PF15	PF16	PF17	PF18	PF19
Hand	924.2	1402.3	560.3	892.4	876.8
Auto	976.7	1431.4	580.0	973.2	968.5

Note. Area is expressed in mm^2.

Surface Area of GM/WM Interface

An intrinsic property of the MPFC is its GM/WM interface. Table 3 compares the surface area of the GM/WM interface of the surfaces extracted from the hand and automated segmentation of brains PF15–PF19. Notice the surface area obtained from the automated segmentation differ from the hand segmentation by an average of 5%. The difference also appears to be a consistent bias between the automated algorithms and the expert rater.

CONCLUSIONS

With these methods we have demonstrated that neuromorphometric parameters associated with the medial prefrontal cortex can be robustly quantified. In this manuscript, we have demonstrated how cortical analysis via an automated Bayesian segmentation methods can be used to quantify regional variables such as volumes of GM, WM, or CSF and to derive profiles of cortical thickness over specific regions.

Although a model-based EM approach that takes into account MRI inhomogeneity and field gain such as that developed by Wells *et al.* (1996) could have been used, the local parametric fitting in our EM algorithm is quite accurate and robust as has been shown in previous work (Joshi *et al.*, 1999; Miller *et al.*, 2000).

It has been shown that including information on partial volumes in the Bayesian segmentation of MR data improves the segmentation and surface reconstruction. Partial volumes arise because the highly curved gyri and sulci of the cortical surface intrinsically results in image voxels sharing characteristics of mixed tissue types (CSF, GM, WM). Further analysis of the partial volume results in a robust segmentation that provides the data for accurate isocontouring used in the surface reconstruction. The resulting segmentation is used to reconstruct a highly detailed and valid surface reconstruction of the GM–WM boundary in order to characterize sulcal and gyral characteristics of specific regions and to compute regional surface area.

We believe this is a first attempt to reconstruct the cortical surface including measures of surface area and cortical thickness metrics of the MPFC giving us a unique computational tool to perform comparative and longitudinal analysis of MPFC neuromorphometry in major depressive disorder and other psychiatric disorders. These methods of quantifying regional cortex characteristics significantly add to the neuromorphometric description of specific regions, taking advantage of other regional characteristics in addition to the traditional description of regional volume. Both triangulated cortical surface and the segmented data have been combined in this paper to determine the surface area of the GM/WM interface in the MPFC. Quantification of these regional parameters is currently in progress to characterize potential changes in medial prefrontal cortex associated with affective disorders in our sample of epidemiologically identified twins.

APPENDIX

Algorithm 2: Cortical Thickness Metric

Denote the set of voxels in the image by V and the set of points in the surface by S.

```
for all $V_i \in V$ do
    $S_{\text{closest}} \leftarrow$ a point in $S$ such that for all $S_i \in S$, distance $(S_{\text{closest}}, V_i) \leq$ distance $(S_i, V_i)$
    $D_i =$ distance $(S_{\text{closest}}, V_i)$
    add $D_i$ to the appropriate histogram
end for
```

Furthermore, finding S_{closest} in the above algorithm is computationally intensive if we compare the distance between every V_i and every S_i as was the case in Miller *et al.* (2000). We now propose a faster and efficient algorithm that does not calculate each distance by appealing to ideas in computer science (Sedgwick, 1983). We begin by organizing the points in S in an OcTree-like structure. We divide the image space in half into $n \times n \times n$ cubes and construct a binary tree with each leaf in the tree representing the space of one cube. Non-leaf nodes represent the space (always a rectangular prism) enclosed by all of the child nodes, and the root note represents the entire image space. We associate a linked list of point coordinates with each node in the tree.

To initialize the tree, we insert each point in S into the tree. Each S_i is added to the linked list corresponding to each node, which represents a space containing S_i. Once the structure has been initialized, we can in most cases find the point in S closest to V_i by examining only a few points. To find S_{closest}, we start at the root node of the tree, and choose the subtree which would contain V_i. We keep going until either we reach a leaf node, or the child node which would contain V_i contains no points. We compute the distance between V_i and each point in the current node's linked list to find the point in the list closest to V_i. We can call this point S_{cur} and, denote the distance from S_{cur} to V_i by D_{cur}.

It is possible that other nodes contain points closer than D_{cur} to V_i. We need to check the points in a leaf node if the corners of the space bounded by that node, or the edges, or the faces, have a distance to V_i less than D_{cur}. Call the set of nodes N, with N_{root} the root node. We check for points in other nodes by constructing a stack of nodes $\mathcal{S}$ via the following algorithm.

Algorithm 3: Finding the Closest Point to V_i

```
Push $N_{\text{root}}$ onto $\mathcal{S}$
while $\mathcal{S}$ is not empty do
    $N_{\text{cur}} \leftarrow (\mathcal{S}.\text{pop}())$
    if $N_{\text{cur}}$ is a leaf then
        for all $P_j$ in $N_{\text{cur}}$'s linked list do
            if distance $(P_j, C_i) \leq D_{\text{cur}}$ then
                $D_{\text{cur}} =$ distance $(P_j, C_i)$
                $S_{\text{cur}} = P_j$
            end if
        end for
    else
        if $N_{\text{cur}} \rightarrow$ right child is within $D_{\text{cur}}$ of $C_i$ then
            $\mathcal{S}$.push $(N_{\text{cur}} \rightarrow$ right child$)$
        end if
        if $N_{\text{cur}} \rightarrow$ left child is within $D_{\text{cur}}$ of $C_i$ then
            $\mathcal{S}$.push $(N_{\text{cur}} \rightarrow$ left child$)$
        end if
    end if
end while
```

When the stack is empty, S_{cur} is S_{closest}, the closest point in the surface S to C_i.

The efficiency of this algorithm is highly dependent on the selection of n, the dimension of the space represented by each leaf node. The n chosen for these brains was 9 voxels, such that each leaf node enclosed a cubic region which was 9 voxels long on each side.

Algorithm 5: Gray Matter/White Matter Interface Surface Area

Let each point on the triangulated graph be denoted by (X_i, Y_i, Z_i), where $i = 1, \ldots, N$, N being the number of points on the graph.

Let $Y_{\mathrm{MAX}} = \max\{Y_i\}$, $Y_{\mathrm{MIN}} = \min\{Y_i\}$ and $Z_{\mathrm{MIN}} = \min\{Z_i\}$.

```
for all triangles do
    For vertices $v_k$, $k = 1, 2, 3$, get labels $S_k \in$ CSF, CSF/GM $-$ PV, GM, GM/WM $-$ PV, WM, intensity $I_k$ and coordinates $x_{v_k}, y_{v_k}, z_{v_k}$.
    Set $IFACE = 0$
    if ($S_1 \neq WM$ & $I_1 > 0$) or ($S_2 \neq WM$ & $I_2 > 0$) or ($S_3 \neq WM$ & $I_3 > 0$) then
        Set $IFACE = 1$
        if $y_{v_1} = Y_{\mathrm{MAX}}$ or $y_{v_2} = Y_{\mathrm{MAX}}$ or $y_{v_3} = Y_{\mathrm{MAX}}$ or $y_{v_1} = Y_{\mathrm{MIN}}$ or $y_{v_2} = Y_{\mathrm{MIN}}$ or $y_{v_3} = Y_{\mathrm{MIN}}$ then
            the triangle is on the first or last sagittal plane facing the background space and thus $IFACE = 0$
        end if
        if $z_{v_1} = Z_{\mathrm{MIN}}$ or $z_{v_2} = Z_{\mathrm{MIN}}$ or $z_{v_3} = Z_{\mathrm{MIN}}$ or $z_{v_3} = Z_{\mathrm{MIN}}$ then
            the triangle is on the first coronal plane facing the background space and thus $IFACE = 0$
        end if
    end if
    if $IFACE = 1$ then
        compute the area of the triangle using $x_{v_k}, y_{v_k}, z_{v_k}$
        add to surface area of interface
    end if
end for
```

ACKNOWLEDGMENTS

The work reported here was supported by NSF-NPACI (J.T.R.), NIH 5-R01-NS35368-05 (M.I.M.), the Mayo Foundation, who provided the Analyze software, K08-MH01292 (K.N.B.), and the Charles F. Dana Foundation "Clinical Hypotheses in Neuroscience Research Program" (R.D.T.). We thank R. E. Hulse for assistance in preparing Figs. 1 and 2 and Dr. M. Hurdal for discussions on the surface area algorithm.

REFERENCES

Bakircioglu, M., Grenander, U., Khaneja, N., and Miller, M. I. 1998. Curve matching on brain surfaces using frenet distances. *Hum. Brain Mapp.* **6:** 329–333.

Bakircioglu, M., Joshi, S. C., and Miller, M. I. 1999. Landmark matching on brain surfaces via large deformation diffeomorphisms on the sphere. In *Medical Imaging 1999: Image Processing* (K. Hanson, Ed.), Vol. 3661, pp. 710–715. SPIE, San Diego, CA.

Botteron, K. N., and Figiel, G. S. 1997. The neuromorphometry of affective disorders. In *Brain Imaging in Clinical Psychiatry* (K. Krishnan, Ed.), pp. 145–184. Dekker, New York, NY.

Botteron, K. N., Raichle, M. E., Drevets, W. C., Heath, A. C., and Todd, R. D. 2001. Volumetric reduction in left subgenual prefrontal cortex in early onset depression. *Biol. Psychiatry,* in review.

Dale, A. M., and Sereno, M. I. 1993. Improved localization of cortical activity by combining EEG and MEG with MRI cortical surface reconstruction—a linear approach. *J. Cogn. Neurosci.* **5:** 162–176.

Drevets, W., and Todd, R. D. 1997. Depression, mania and related disorders. In *Adult Psychiatry* (S. B. Guze, Ed.), pp. 99–142. Mosby, St. Louis, MO.

Drevets, W. C. 1999. Prefrontal cortical-amygdalar metabolism in major depression. *Ann. N. Y. Acad. Sci.* **877:** 614–637.

Drevets, W. C., and Botteron, K. N. 1996. Neuroimaging in psychiatry. In *Adult Psychiatry* (S. B. Guze, Ed), pp. 53–81. Mosby, St. Louis, MO.

Drevets, W. C., Price, J. L., Simpson, J. R., Todd, R. D., Reich, T., Vannier, M., and Raichle, M. E. 1997. Subgenual prefrontal cortex abnormalities in mood disorders. *Nature* **386:** 824–827.

Drevets, W. C., Videon, T. O., Price, J. L., Preskorn, S. H., Carmichael, S. T., and Raichle, M. E. 1992. A functional anatomical study of unipolar depression. *J. Neurosci.* **12:** 3628–3641.

Drury, H. A., VanEssen, D. C., Anderson, C. H., Lee, C. W., Coogan, T. A., and Lewis, J. W. 1996. Computerized mappings of the cerebral cortex: A multiresolution flattening method and a surface-based coordinate system. *J. Cogn. Neurosci.* **8:** 1–28.

Grabowski, T. J., Frank, R. J., Szumski, N. R., Brown, C. K., and Damasio, H. 2000. Validation of partial tissue segmentation of single-channel magnetic resonance images of the brain. *Neuroimage* **12:** 640–656.

Grenander, U., and Miller, M. I. 1998. Computational anatomy: An emerging discipline. *Quart. Appl. Math.* **56:** 617–694.

Gueziec, A., and Hummel, R. 1995. Exploiting triangulated surface extraction using tetrahedral decomposition. *IEEE Trans. Vis. Comp. Graph.* **1:** 328–334.

Haller, J. W., Banerjee, A., Christensen, G. E., Gado, M., Joshi, S., Miller, M. I., Sheline, Y., Vannier, M. W., and Csernansky, J. G. 1997. Three-dimensional hippocampal MR morphometry with high-dimensional transformation of a neuroanatomic atlas. *Radiology* **202:** 504–510.

Hirayasu, Y., Shenton, M. E., Salisbury, D. F., Kwon, J. S., Wible, C. G., Fischer, I. A., Yurgelun-Todd, D., Zarate, C., Kikinis, R., Jolesz, F. A., and McCarley, R. W. 1999. Subgenual cingulate cortex volume in first-episode psychosis. *Am. J. Psychiatry* **156:** 1091–1093.

Holmes, C. J., Hoge, R., Woods, R. P., Evans, A. C., and Toga, A. 1998. Enhancement of MR images using registration for signal averaging. *J. Comput. Assist. Tomogr.* **22:** 324–333.

Joshi, M., Cui, J., Doolittle, K., Joshi, S., Van Essen, D., Wang, L., and Miller, M. I. 1999. Brain segmentation and the generation of cortical surfaces. *Neuroimage* **9:** 461–476.

Kapur, T., Grimson, W. E. L., Wells, W. M., III, and Kikinis, R. 1996. Segmentation of brain tissue from magnetic resonance images. *Med. Image Anal.* **1:** 109–127.

Khaneja, N., Miller, M. I., and Grenander, U. 1998. Dynamic programming generation of curves on brain surfaces. *IEEE Trans. Pattern Anal. Mach. Intell.* **20:** 1260–1265.

Mayberg, H. S., Liotti, M., Brannan, S. K., McGinnis, S., Mahurin, R. K., Jerabek, P. A., Silva, J. A., Tekell, J. L., Martin, C. C., Lancaster, J. L., and Fox, P. T. 1999. Reciprocal limbic-cortical function and negative mood: converging pet findings in depression and normal sadness. *Am. J. Psychiatry* **156:** 675–682.

Miller, M. I., and Massie, A. B., Ratnanather, J. T., Botteron, K. N., and Csernansky, J. G. 2000. Bayesian construction of geometrically based cortical thickness metrics. *Neuroimage* **12:** 676–687.

Murray, C. J., and Lopez, A. D. 1996. Evidence-based health policy—Lessons from the global burden of disease study. *Science* **274:** 740–743.

Ongur, D., Drevets, W. C., and Price, J. L. 1998. Glial reduction in the subgenual prefrontal cortex in mood disorders. *Proc. Nat. Acad. Sci. USA* **95:** 13290–13295.

Rajkowska, G., Miguel-Hidalgo, J. J., Wei, J., Dilley, G., Pittman, S. D., and Meltzer, H. Y. 1999. Morphometric evidence for neuronal and glial prefrontal cell pathology in major depression. *Biol. Psychiatry* **45:** 1085–1098.

Robb, R. A. 1999. *Biomedical Imaging, Vizualization and Analysis.* Wiley, New York, NY.

Sedgwick, R. 1987. *Algorithms.* Addison-Wesley, Boston, MA.

Soares, J. C., and Mann, J. J. 1997. The anatomy of mood disorders—Review of structural neuroimaging studies. *Biol. Psychiatry* **41:** 86–106.

Swerdlow, N. R., and Koob, G. F. 1987. Dopamine, schizophrenia, mania and depression: Toward a unified hypothesis of cortico-striato-pallido-thalamic function. *Behav. Brain Sci.* **10:** 197–245.

Teo, P. C., Sapiro, G., and Wandell, B. A. 1997. Creating connected representations of cortical gray matter for functional mri visualization. *IEEE Med. Transactions* **16:** 852–863.

Thompson, P. M., Schwartz, C., Lin, R. T., Khan, A. A., and Toga, A. W. 1996. Three-dimensional statistical analysis of sulcal variability in the human brain. *J. Neurosci.* **16:** 4261–4274.

Wells, W. M., III, Grimson, W. E. L., Kikinis, R. L., and Jolesz, F. A. 1996. Adaptive segmentation of MRI data. *IEEE Trans. Med. Imag.* **15:** 429–442.

Xu, C., Pham, D. L., Rettmann, M. E., Yu, D. N., and Prince, J. L. 1999. Reconstruction of the human cerebral cortex from magnetic resonance images. *IEEE Trans. Med. Imag.* **18:** 467–480.